Physics of the Earth and Planetary Interiors 245 (2015) 1–14

Contents lists available at ScienceDirect

Physics of the Earth and Planetary Interiors

journal homepage: www.elsevier.com/locate/pepi

Mid-mantle seismic anisotropy beneath southwestern Pacific subduction systems and implications for mid-mantle deformation

Anwar Mohiuddin *, Maureen D. Long, Colton Lynner

Department of Geology and Geophysics, Yale University, New Haven, CT, United States

ARTICLE INFO

Article history:
Received 19 February 2015
Received in revised form 7 May 2015
Accepted 7 May 2015
Available online 18 May 2015

Keywords:
Mid-mantle
Seismic anisotropy
Subduction zones
Shear wave splitting
Mantle deformation

ABSTRACT

Observations of seismic anisotropy can offer relatively direct constraints on patterns of mantle deformation, but most studies have focused on the upper mantle. While much of the lower mantle is thought to be isotropic, several recent studies have found evidence for anisotropy in the transition zone and uppermost lower mantle (the mid-mantle), particularly in the vicinity of subducting slabs. Here we investigate anisotropy at mid-mantle depths in the Tonga-Kermadec, Sumatra, New Britain, New Hebrides, and Philippines subduction zones using the source-side shear wave splitting technique. We measure splitting of direct teleseismic S phases originating from deep events (>300 km) that have been corrected for the effect of upper mantle anisotropy beneath the seismic stations. We find evidence for considerable anisotropy at mid-mantle depths in all subduction systems studied, with delay times averaging ~1.0–1.5 s. Several measurements originating from depths greater than 600 km exhibit delay times greater than 1 s, suggesting a significant contribution from anisotropy in the uppermost lower mantle. We combine our results with those documented in previous studies into a quasi-global set of source-side shear wave splitting measurements that reflect mid-mantle anisotropy. We document significant variability in the dominant fast directions both within and among individual subduction systems, suggesting different deformation geometries among different subduction systems. As further constraints on the elasticity and deformation of mid-mantle minerals become available, our dataset can be used to constrain patterns of mid-mantle flow associated with subduction.

© 2015 Elsevier B.V. All rights reserved.

1. Introduction

The dynamic interaction between subducting slabs and the mantle transition zone represents a fundamental unsolved problem. The sinking of slabs across the 660 km discontinuity plays a key role in mass transfer between the surface and the deep mantle, but the details of this process remains poorly understood. High-resolution tomographic images of subducting slabs reveal that slabs interact with the transition zone in different ways, with some slabs stagnating in or beneath the transition zone and others apparently penetrating to the lower mantle without much deformation (van der Hilst et al., 1991; Fukao et al., 1992; Karason and van der Hilst, 2000; Fukao and Obayashi, 2013). This variability in style of subduction implies varying patterns of mid-mantle deformation associated with slabs impinging upon or penetrating into the lower mantle. Observations of seismic anisotropy at mid-mantle depths can provide constraints on these patterns of mid-mantle deformation.

Most mantle minerals are elastically anisotropic, and aggregates of such minerals, when subjected to deformation in the dislocation creep regime, develop a crystallographic preferred orientation (CPO) resulting in bulk seismic anisotropy (Karato and Wu, 1993). In addition to CPO, shape preferred orientation (SPO), or the alignment of elastically distinct materials, could also develop from deformation and produce bulk seismic anisotropy. The mantle transition zone is characterized by a series of phase transitions, with associated discontinuities in seismic velocity structure. At a depth of ~410 km, olivine transforms to wadsleyite (Anderson, 1967), which has an intrinsic shear wave anisotropy of ~16.5% (Zha et al., 1997; Mao et al., 2008); CPO of deformed wadsleyite thus may contribute to transition zone anisotropy. Demouchy et al. (2011) reported weak CPO in deformed wadsleyite, and Smyth et al. (2012) suggested that wadsleyite CPO can be partially inherited from pre-transformation olivine textures. Kawazoe et al. (2013) recently performed deformation experiments on wadsleyite at transition zone conditions, demonstrating that wadsleyite aggregates may develop a preferred orientation. At a depth of ~520 km, wadsleyite transforms to ringwoodite; estimates for the single crystal shear wave anisotropy of ringwoodite

* Corresponding author.
E-mail address: anwar.mohiuddin@yale.edu (A. Mohiuddin).

http://dx.doi.org/10.1016/j.pepi.2015.05.003
0031-9201/© 2015 Elsevier B.V. All rights reserved.

range from ~3% to 8% (Karki et al., 2001; Li et al., 2006; Wang et al., 2006; Mainprice, 2007). Polycrystalline aggregates of ringwoodite are expected to develop only weak anisotropy (less than 1%; Wenk et al., 2005).

The uppermost lower mantle (below the 660 km discontinuity) is mainly composed of bridgmanite (magnesium silicate perovskite; Tschauner et al., 2014). Single crystals of bridgmanite are anisotropic at mid-mantle conditions, with shear wave anisotropies up to ~10–12% (Karki et al., 1997; Mainprice et al., 2000; Wentzcovitch et al., 2004). Theoretical modeling and laboratory experiments show that CPO might develop in this mineral if dislocation creep dominates (Cordier et al., 2004; Wenk et al., 2006). Work by McNamara et al. (2003) suggested that when the strain rate is large, as might be expected for flow around a subducting slab, a local change of deformation mechanism from diffusion creep to dislocation creep may take place, resulting in CPO anisotropy of bridgmanite. However, the deformation mechanisms and CPO patterns for bridgmanite remain poorly constrained. In addition to bridgmanite, the lower mantle contains ~20% ferropericlase (e.g., Bass and Parise, 2008). At uppermost lower mantle conditions ferropericlase is nearly isotropic (Marquardt et al., 2009), although a small contribution to anisotropy from SPO of deformed ferropericlase grains may be possible at these conditions.

Measurements of seismic anisotropy can constrain patterns of deformation in the mantle. To analyze and quantify the nature of anisotropy, a useful tool is shear wave splitting analysis, in which the orientation of the fast polarized wave (φ) and the delay time between the fast and slow polarized wave (δt) are measured. In the upper mantle, the geometrical relationships between deformation geometry and the resulting fast splitting directions are relatively well known (e.g. Karato et al., 2008). In contrast, these relationships remain imperfectly understood for transition zone and uppermost lower mantle minerals. Despite this limitation, measurements of shear wave splitting due to mid-mantle anisotropy have the potential to offer insights into the strength, geometry, and variability of deformation around slabs. One strategy for examining mid-mantle anisotropy is the measurement of source-side shear wave splitting (e.g., Russo and Silver, 1994). This technique leverages the abundant seismicity of subduction zones to examine anisotropy near these seismic sources. In order to isolate shear wave splitting in the source region, any contribution to splitting from anisotropy beneath a seismic station must be removed.

Several studies have documented seismic anisotropy at mid-mantle depths using both body waves (Wookey et al., 2002; Chen and Brudzinski, 2003; Wookey and Kendall, 2004; Foley and Long, 2011; Di Leo et al., 2012; Lynner and Long, 2014; Nowacki et al., 2015) and surface waves (Trampert and van Heijst, 2002; Yuan and Beghein, 2013), although they are not plentiful compared to studies of upper mantle anisotropy. Global models by Trampert and van Heijst (2002) using dispersion measurements of Love wave overtones suggested the global presence of azimuthal anisotropy in the transition zone. Later work by Yuan and Beghein (2013) using Rayleigh wave phase velocity also reported the presence of significant anisotropy in the transition zone, with changes in anisotropy across the transition zone discontinuities. The long period surface waves used in these studies limit the spatial resolution, however, precluding the characterization of small-scale features in subduction systems.

Tonga is the only subduction system in which mid-mantle anisotropy has been studied extensively to date by multiple authors; Chen and Brudzinski (2003) and Wookey and Kendall (2004) documented anisotropy in the transition zone below and above the subducting Tonga slab respectively. Later measurements by Foley and Long (2011) of source-side splitting for direct S phases from events in Tonga argued for anisotropy in the sub-slab mantle at both transition zone depths and in the uppermost lower mantle, with delay times of ~1 s attributed to mid-mantle anisotropy. Using a similar technique but a different set of events and raypaths, Kaneshima (2014) argued that anisotropy in the upper-most lower mantle just to the north of Tonga is negligible. Finally, Nowacki et al. (2015) also applied the source-side splitting technique and argued for the presence of significant anisotropy at mid mantle depths in northern Tonga, suggesting that the anisotropy originates from hydrous phases within the slab.

Given these previous suggestions of mid-mantle anisotropy at both global and regional scales, it is timely to examine whether mid-mantle anisotropy is a ubiquitous feature in subduction systems. Well-documented patterns of mid-mantle anisotropy near subducting slabs would provide valuable constraints on patterns of deformation in the mid-mantle and could potentially constrain global models for mantle convection and material transport. Here we build on previous work in Tonga and elsewhere (e.g., Foley and Long, 2011; Di Leo et al., 2012; Kaneshima, 2014; Lynner and Long, 2014, 2015; Nowacki et al., 2015) and present measurements of source-side shear wave splitting from deep earthquakes originating in the Tonga-Kermadec, Sumatra, New Britain, New Herbides, and Philippines subduction systems. We interpret these measurements as reflecting anisotropy in the transition zone and uppermost lower mantle. In addition, we compile results from previous studies using identical station selection, data processing, and measurement techniques (Foley and Long, 2011; Lynner and Long, 2014, 2015). Using our quasi-global compilation, we address the following queries: What is the source of mid-mantle anisotropy in subduction systems worldwide? What mineral phases contribute to the observed anisotropy? Is there variability in the strength or geometry of anisotropy either within or among different subduction systems? Do the observed patterns of anisotropy depend on slab morphology or kinematics? The ultimate goal of this research effort is to combine observations of mid-mantle anisotropy with improved constraints on the elasticity and deformation of mid-mantle minerals to gain insight into patterns of flow in the mid-mantle in subduction systems.

2. Tectonic setting of the study areas

Ample deep seismicity (event depths >300 km, Fig. 1) in the New Hebrides, New Britain, Sunda-Banda, Philippines, and Tonga regions make them ideal regions in which to study mid-mantle anisotropy though measurements of source-side shear wave splitting. Here we briefly review the tectonic setting of each region. Beneath Tonga, old (>120 Myr) Pacific plate is subducting to the west beneath the Australian plate at a rate of >100 mm/yr (Schellart et al., 2008; van der Hilst, 1995). Slab contours derived from seismicity (Gudmundsson and Sambridge, 1998) show that the slab has a curved geometry at the trench and the slab curvature increases with depth. Tomographic images, in which slabs appear as positive (fast) velocity anomalies, reveal that in the northern region the slab stagnates above the 660 km discontinuity (e.g., Fukao and Obayashi, 2013). Toward the south in the Kermadec subduction zone, however, the slab anomaly appears to penetrate the transition zone and stagnate in the uppermost lower mantle, at a depth of ~1000 km (Fukao and Obayashi, 2013). The trench migration behavior is also variable along strike: in the Kermadec region the trench is advancing (~40 mm/yr) in a Pacific hotspot reference frame (HS3-NUVEL1A; Gripp and Gordon, 2002), while to the north, rapid trench retreat (>100 mm/yr) is observed (Schellart et al., 2008).

The New Hebrides subduction system encompasses the subduction of the Indo-Australian plate beneath the New Hebrides arc to

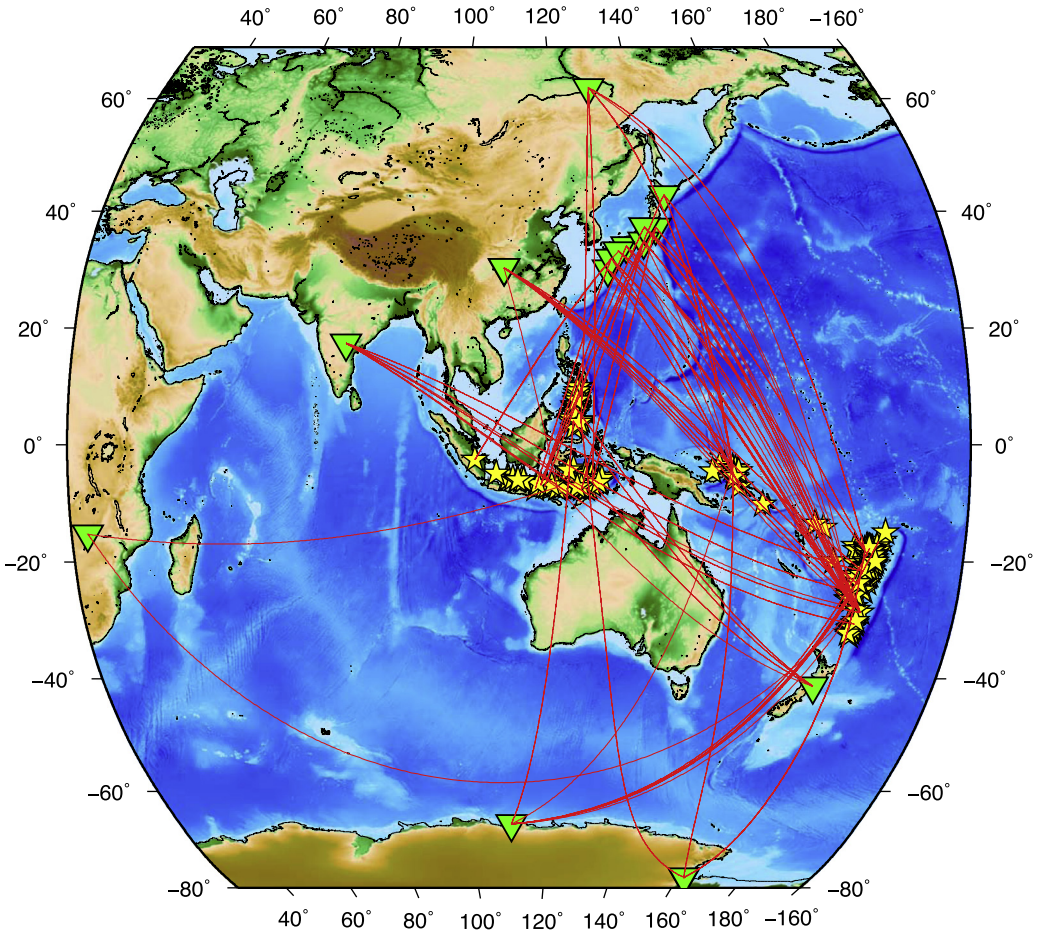

Fig. 1. Locations of events (yellow stars) and stations (green triangles) used in this study. To show ray path coverage, we show a few great circle paths connecting event and station locations as thin red lines. (For interpretation of the references to color in this figure legend, the reader is referred to the web version of this article.)

the northeast at a rate of ∼100 mm/yr (Schellart et al., 2008). The age of the subducting plate varies from 45 Myr in the south to 60 Myr in the north. No systematic change in trench retreat with age is observed as the trench retreats at an average trench normal rate of ∼60 mm/yr (Heuret and Lallemand, 2005; Schellart et al., 2008). Tomographic images reveal a flat lying fast anomaly in the upper mantle (Hall and Spakman, 2003). Although weak fast anomalies are found in the uppermost lower mantle (∼700 km), the limited resolution cannot resolve whether the slab has penetrated to the lower mantle (Hall and Spakman, 2003). However, the presence of seismicity at depths to ∼660 km provides evidence that the slab penetrates at least to the base of the transition zone.

The New Britain subduction zone lies to the north of New Hebrides Subduction system. This area is tectonically complicated, with several subducting plates (the North Bismark, South Bismark, Solomon Sea, Woodlark, and Manus microplates). Based on published slab morphology models derived from seismicity, the events used in our study originate within the subducting Solomon Sea plate as it dips to the north beneath the South Bismark plate (Bird, 2003). In the north, the trench is advancing at 10 mm/yr, but in the southern region the trench retreats at a rate of 18 mm/yr (Heuret and Lallemand, 2005). Tomography reveals clear evidence of slab material in the upper mantle; the slab geometry at depth roughly follows the cusp of the trench (Hall and Spakman, 2003), but fast velocity anomalies related to the cold downwelling slab become diffuse and difficult to interpret beyond 440 km (Hall and Spakman, 2003) making the nature of the slab interaction (stagnant/non-stagnant) with the transition zone elusive.

The Moluccan (Philippines) subduction zone lies in the area of a complex junction between the Eurasian, Australian, Pacific and Philippine Sea plates (Fig. 1). The slab is 1100 km wide along strike and has a curved geometry at the trench, dipping to the west, with trench advance rates of ∼ 25 mm/yr (Schellart et al., 2008). Early studies of slab seismicity suggested the presence of two Wadati-Benioff zones dipping in opposite directions (Silver and Moore, 1978); this finding was later confirmed using seismic tomography (Widiyantoro and van der Hilst, 1997). The west-dipping slab is steeper than the east-dipping slab and it penetrates through the transition zone without much apparent deformation (Widiyantoro and van der Hilst, 1997). The east-dipping slab does not have deep seismicity and therefore our results are from the west-dipping branch of this subduction zone.

Beneath Sumatra, the Australian plate is subducting beneath the Sunda plate, accommodating its northward motion toward Eurasia. The slab is dipping northeastward and the arc is curved, such that the subduction obliquity changes from east to west. The interaction of the subducting plate with the transition zone is variable along strike (Fukao and Obayashi, 2013). In the eastern region, the subducting plate lies flat above the 660 km discontinuity, whereas in the central region the slab seems to penetrate the 660 and in the western region the slab appears to stagnate in the uppermost lower mantle (Fukao and Obayashi, 2013). On average, trench advance of ∼15 mm/yr is observed (Heuret and Lallemand, 2005); this rate is slightly faster in the east and slower in the west. The slab is youngest in the west (∼50 Myr) and ages to the east (>100 Myr) (Heuret and Lallemand, 2005; Müller et al., 2008).

3. Data and methods

3.1. Measurement strategy and station selection

In this study we use the source-side shear wave splitting technique (Vinnik and Kind, 1993; Russo and Silver, 1994, and later studies), which uses direct teleseismic S phases originating from earthquakes within subducting slabs. As shear wave splitting is a path-integrated phenomenon, anisotropy from both the source-side and the receiver-side may contribute to the splitting signal measured at the station. To constrain the anisotropy accumulated in the mantle near the source, we restrict our analysis to stations at which the upper mantle anisotropy beneath the receiver is well characterized. A simple pattern of shear wave splitting indicates either a single horizontal layer of anisotropy or an apparently isotropic upper mantle. Measurements of splitting of the direct S phase are corrected for the effect of anisotropy beneath the receiver, and the remaining signal is attributed to anisotropy near the source. A schematic of the source side measurement method is shown in Fig. 2.

To characterize receiver side anisotropy we used SKS, SKKS, and PKS (later referred to as *KS) phases arriving at epicentral distances between 90° and 130° over a range of backazimuths, measured at periods between 8 and 25 s, following previous work (Lynner and Long, 2013, 2014). We restricted our analysis to stations that show either an apparently null *KS splitting pattern (that is, a large number of non-split *KS arrivals over a large backazimuthal swath, with few or no split arrivals) or a simple *KS splitting pattern (with consistent splitting parameters measured for multiple backazimuthal ranges). We ensured that each station had backazimuthal coverage sufficient to show consistent null or simple splitting in at least two quadrants. Any station with insufficient backazimuthal coverage or splitting that varied with backazimuth was not used (further details of receiver-side anisotropy corrections can be found in Lynner and Long, 2014). While this conservative approach to station selection may limit the number of stations we can use in our study, it also minimizes potential errors due to inaccurate receiver-side corrections, as we only use stations for which we are highly confident in our ability to correct for upper mantle anisotropy on the receiver side.

For several stations used in this study, upper mantle anisotropy patterns were characterized in previous studies (Lynner and Long, 2013, 2014) using identical techniques. In addition to these, we also examined more than 50 additional long-running broadband stations to expand the pool of available stations (Supplementary Table S1). Of these, only 5 stations exhibited either null (coherent null splitting across all backazimuths) or simple (coherent fast direction and delay time across all backazimuths) splitting. We also used 8 stations of the F-net network characterized in detail by Long and van der Hilst (2005), who found delay times <0.4 s using the multichannel measurement method. We treat these F-net stations as effectively null stations here because a delay time <0.4 s cannot be resolved by our measurement methods at the periods under study. A map of the stations analyzed in this study, with stations used for the source-side splitting measurements highlighted, is shown in Fig. 1. An example receiver-side splitting pattern for a station with apparently null splitting is shown in Fig. 3; splitting patterns for a larger number of stations used in this study are shown in Supplementary Fig. S1.

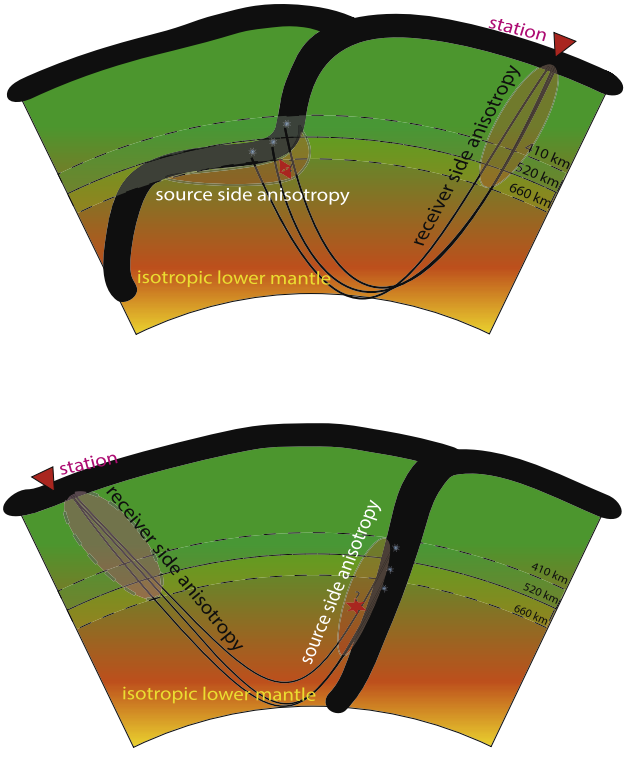

Fig. 2. Schematic cartoons illustrating the source-side shear wave splitting technique, with two different end-member subduction geometries (stagnant, top, vs. non stagnant, bottom). Blue circles indicate event locations; lines indicate schematic raypaths connecting the sources to the station (red triangles). Shaded orange regions indicate possible regions of anisotropy near the source and receiver. (For interpretation of the references to color in this figure legend, the reader is referred to the web version of this article.)

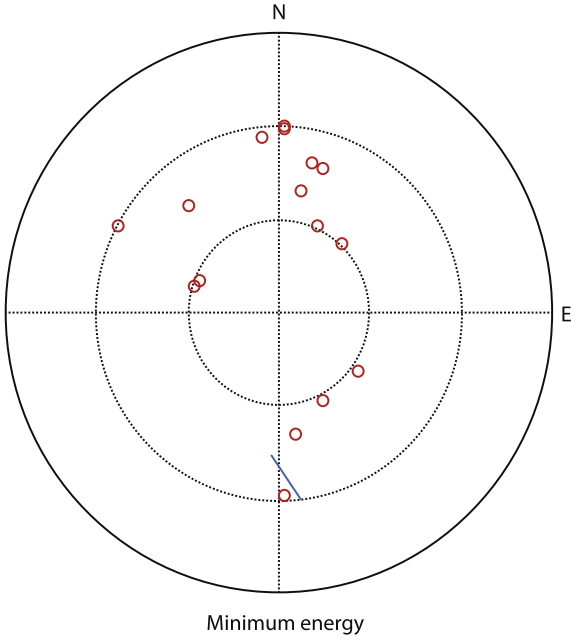

Fig. 3. Example stereoplot of an SKS splitting pattern at a station (CASY, located in Casey, Antarctica) we categorize as a "null" station. Measurements are plotted as a function of backazimuth (clockwise from top of circle) and incidence angle (distance from center of circle). Red circles indicate null measurements; blue bar indicates a split measurement, with the length and orientation of the bar corresponding to the delay time and fast direction, respectively. CASY exhibits well-resolved nulls over a large range of backazimuths, with a single split measurement originating from the south. We interpret this pattern as reflecting apparently isotropic upper mantle beneath the station, with the single split arrival reflecting a localized contribution from anisotropy in the lower mantle or in the shallow mantle or crust beneath the station. (For interpretation of the references to color in this figure legend, the reader is referred to the web version of this article.)

For direct S splitting measurements at stations that exhibit an apparently isotropic upper mantle, we need not make any corrections for receiver side anisotropy. All of the new measurements presented in this study were made using data from apparently null stations, so no receiver-side corrections were made. For the direct S splitting measurements that we compile from the work of Lynner and Long (2014, 2015), some stations with simple *KS splitting patterns were used. For these stations, the authors applied a correction to all S phases to account for upper mantle anisotropy by rotating and time-shifting the horizontal components to account for the upper mantle splitting parameters (e.g., Russo et al., 2010; He and Long, 2011) before measuring the splitting due to source-side anisotropy.

3.2. Shear wave splitting measurements

We measured the splitting of teleseismic S phases originating from deep earthquake sources (depth > 300 km and magnitude > 5.5) in the Sumatra-Indonesia, Philippines, New Hebrides and Tonga subduction zones. To avoid contamination of data from S-to-P conversions near the receiver-side as well as any contribution from lowermost mantle anisotropy, direct S phases with epicentral distances of 40–80° were selected for measurement (Savage, 1999). We used the SplitLab software for preprocessing and splitting measurements (Wüstefeld et al., 2008). We applied a bandpass filter to each waveform, retaining energy between 8 and 25 s; the same filter was used in the receiver-side *KS analysis.

We made splitting measurements on all direct S phases by applying two measurement methods simultaneously (the eigenvalue method and the rotation-correlation method), following previous studies (Lynner and Long, 2013, 2014). We manually chose measurement windows, evaluated measurement quality, and categorized each measurement as "good," "fair," or "poor," according to the following criteria. A "good" measurement was characterized by high signal to noise ratios (>4), elliptical uncorrected particle motion, linear corrected particle motion with the fast direction along the long axis of the ellipse, small and nearly elliptical error spaces, and good agreement between the two measurement methods for both the fast direction and delay time. Typically the splitting measurements for S arrivals rated "good" have errors on rotation-correlation fast directions of less than approximately ± 15° and delay time of less than ±0.5 s. Measurements rated "fair" have relatively large errors, i.e. ±15 – 25° for φ and ±0.5 – 0.9 s for δt. For F-net stations, any measurement with a delay time less than 0.8 s is considered to be below our threshold for null splitting. Any measurement with an error in δt of $\geqslant$1 s and in $\varphi \geqslant 25°$ was marked as "poor". We also characterized direct S phases that had not been split as null arrivals, based on the linearity of the particle motion. Examples of a "good" null direct S arrival and a "good" non-null S splitting measurement are shown in Figs. 4 and 5, respectively. Null measurements may reflect isotropic mantle near the source, if the initial polarization directions are distributed over a wide azimuthal swath, or they may reflect initial polarization directions that are aligned close to the fast or slow splitting direction of the anisotropic medium.

4. Results

We present a total of 217 new measurements in this study, including 76 non-nulls and 141 nulls. We document significant splitting due to anisotropy in the transition zone and/or uppermost lower mantle in each of the regions studied here, with each region exhibiting variability in anisotropy patterns along the trench. Maps of individual splitting measurements of "good" and "fair" quality for each region study areas are shown in Figs. 6–9. Waveforms and diagnostic plots for multiple deep (>400 km) direct S "good" splitting measurements are shown in Fig. S2. All individual measurements, along with error estimates and quality ratings, are reported in Supplementary Table S2.

Due to its abundant seismicity, Tonga has the largest number of results (Fig. 6). We obtained robust measurements for 146 S phases originating beneath Tonga, including 49 splits (21 "good", 22 "fair", and 6 "poor" quality) and 97 nulls (18 "good", 56 "fair", 23 "poor" quality). The split S phases originated from a range of depths

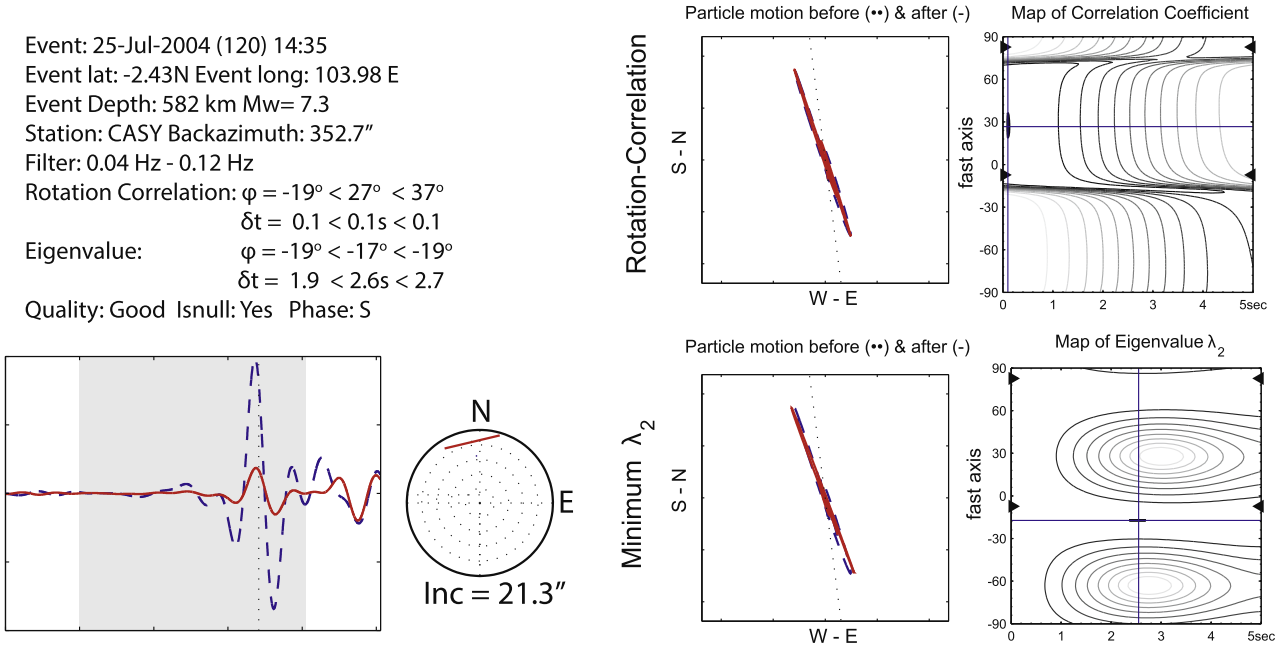

Fig. 4. An example of a "good" null S measurement made at station CASY. Information such as event date, depth, back-azimuth, location, filter used, associated fast direction and delay time is given. For this example the event depth is 582 km. Figure shows uncorrected waveform and a stereoplot showing the backazimuth and incidence of the incoming wave at the station (bottom left). Uncorrected (dashed blue line) and corrected (solid red line) particle motion is shown in the middle column and a map of confidence interval (95% error region for the measurement) for splitting parameters for both rotation correlation and eigenvalue methods is shown in the right most column. (For interpretation of the references to color in this figure legend, the reader is referred to the web version of this article.)

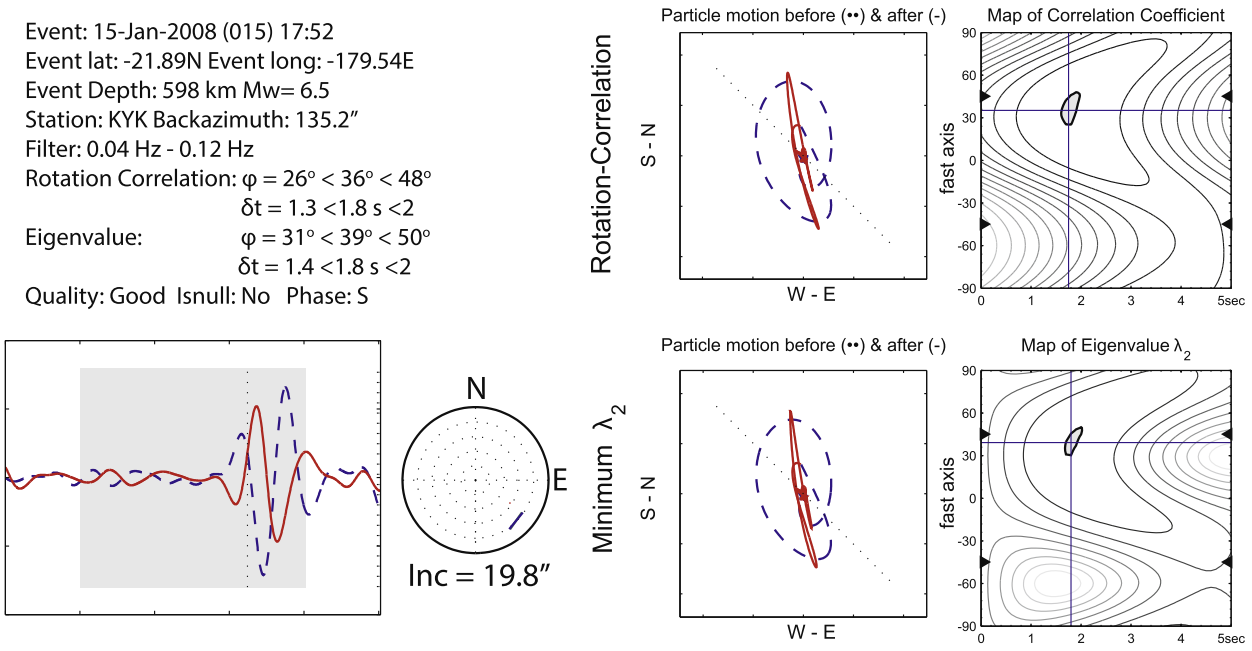

Fig. 5. An example of a "good" quality direct S phase splitting measurement made at station KYK. For this example the event depth is 598 km. Plotting conventions are as in Fig. 4.

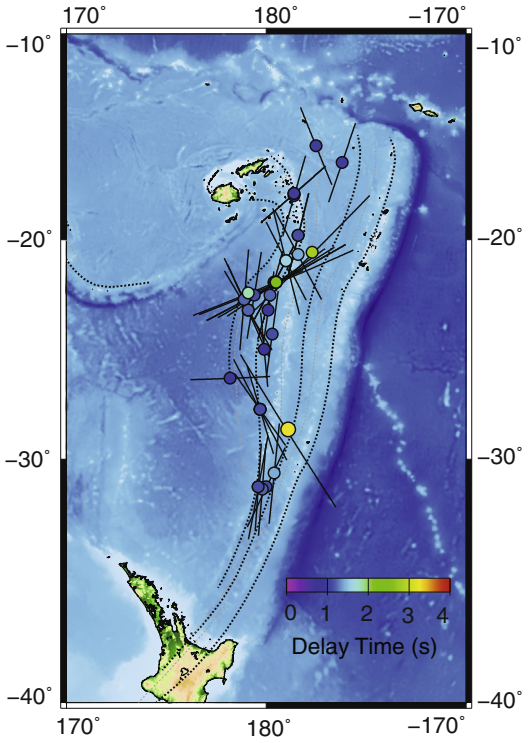

Fig. 6. Splitting results for Tonga shown in map view. Circles are plotted at event locations and color coded by observed delay time. The length and the orientation of the bar correspond to observed delay times and fast directions, respectively. Fast directions measured at the station have been rotated into the coordinate system of the downgoing ray by reflecting the fast direction across the vector representing the great circle path of ray propagation (see, e.g., Foley and Long, 2011; Lynner and Long, 2013, 2014). All "good" and "fair" quality split measurements are shown. The dashed lines are slab contours at 100 km intervals, to a depth of 700 km, from Gudmundsson and Sambridge (1998). (For interpretation of the references to color in this figure legend, the reader is referred to the web version of this article.)

(400–650 km), including at the base of the transition zone. For example, one event originating at a depth of 619 km measured at station TSA in Japan exhibited strong splitting with a delay time of 1.3 s. The average delay time from this region is ~1.3 s. A map of null measurements (Fig. 7) shows that the ratio of split to null measurements is low in the north and increases to the south, with null measurements dominating in the northern region. The fast directions (rotated into the coordinate system of the downgoing ray at the source and plotted at the earthquake location; see figure caption for details) are generally parallel to the slab geometry (from slab contours of Gudmundsson and Sambridge, 1998) of the slab in the mantle. The S wave polarizations of "good", "fair" and "poor" null arrivals generally lie (sub-)parallel to (or sub-perpendicular to) measured fast splitting directions, but the scatter in the null polarization directions is considerably higher than the scatter in φ (Fig. 7). We also observe more scatter in the null directions in the northern portion of the subduction zone than the southern portion.

Beneath Sumatra, we obtained 35 results, including 10 splits and 25 nulls (Fig. 8). Of the split S arrivals, 5 measurements were rated "good," 1 "fair," and 4 "poor." 7 out of 25 nulls were rated as "good", 11 as "fair" and 7 as poor. In this region, we observe well-constrained δt values as high as 3.5 s from events at depths of about 400 km. Even the deepest (587 km) splitting measurement beneath this region (rated "good") accumulated a delay time of 1.5 s. Deep splitting measurements from the eastern and western portions of Sumatra exhibit contrasting fast direction. To the west, we observe mainly trench parallel fast directions (Fig. 8) that transition to trench perpendicular φ in the east. In comparison to Tonga, we do not have as many null measurements in Sumatra but in general the polarizations of "good" and "fair" null measurements generally align with fast splitting directions. As in Tonga, the scatter in polarization directions for null arrivals is considerably higher than the scatter in φ.

New Hebrides, to the north of Tonga, has much less deep seismicity than Tonga and therefore only one "good" result was obtained (Fig. 9), with a trench perpendicular fast direction.

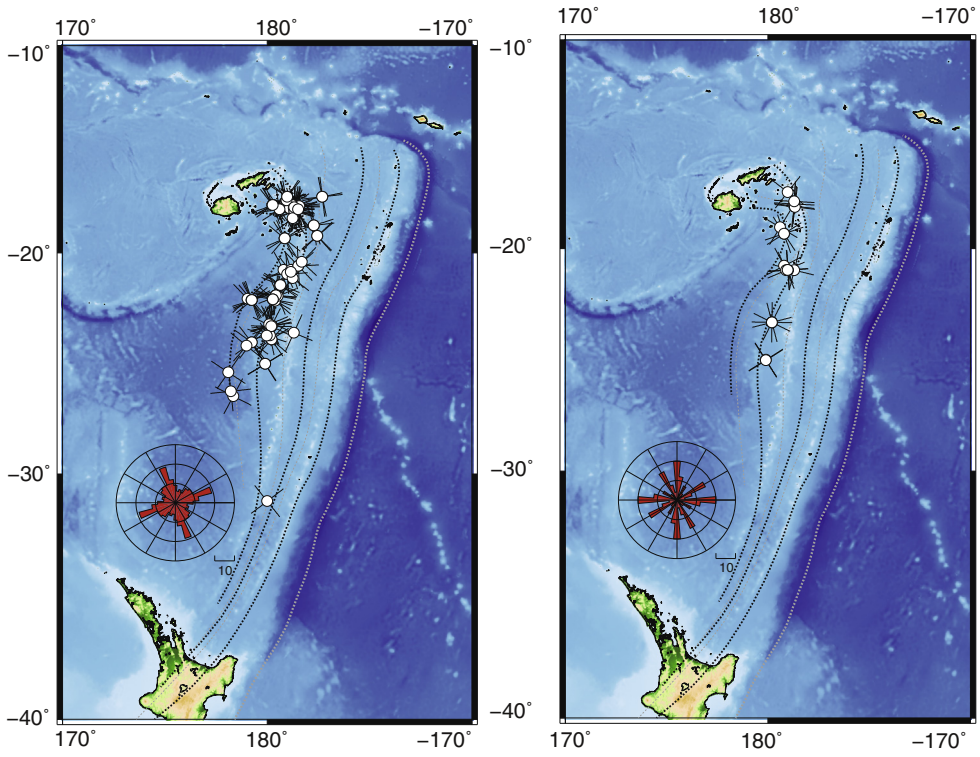

Fig. 7. All null splitting results for Tonga shown in map view (left); measurements of "good" quality are shown on the right. Bars are aligned in the initial polarization direction of the linearly polarized S arrival and in the direction orthogonal to the initial polarization. The rose diagram on the inset shows a circular histogram of the distribution of incoming polarization directions.

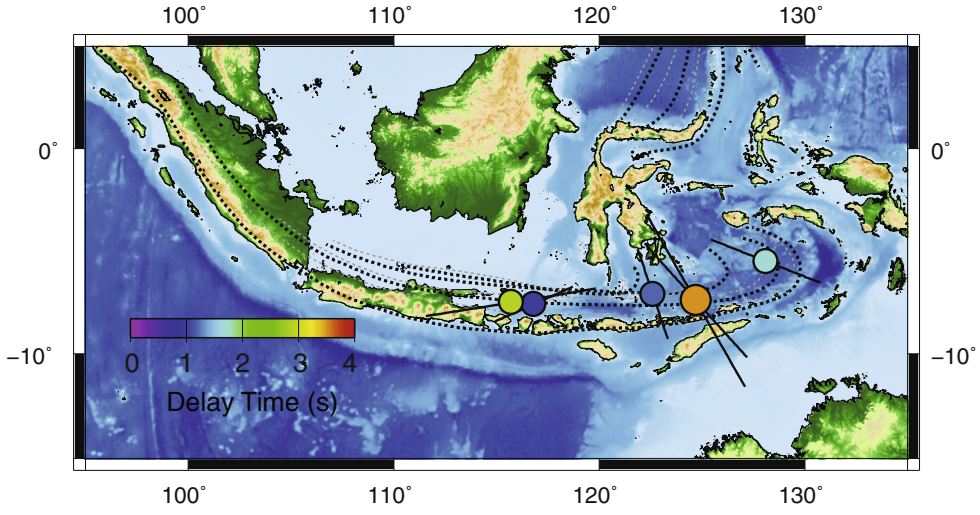

Fig. 8. Sumatra splitting results. Plotting conventions are as in Fig. 6.

Notably, we observe a good quality split with a well-constrained delay time of 1.2 s from an event at a depth of 667 km, at the very base of the transition zone, indicating the presence of anisotropy in the uppermost lower mantle. We obtained 12 results for the New Britain subduction zone, of which there are 9 splits and 3 nulls. Of those, 4 are rated "good", 3 "fair," and 2 "poor." In contrast to New Hebrides, the New Britain region exhibits generally trench-parallel fast directions (Fig. 9) and an average delay time of 1.4 s. Specifically, as the rated quality goes from "good" to "poor", the variability in the fast direction increases; the highest-quality results are generally trench-parallel. There is some scatter in the fast directions near the "cusp" of the trench where the slab curvature is high (Fig. 9). The deepest split S wave we measured from this region originated from 420 km depth and yields a "good" quality measurement with a δt of 1.8 s. Measured delay times vary between 0.9 and 3 s (shallowest event ~379 km). There are only a few "fair" and "poor" quality null measurements on New Hebrides and New Britain regions; beneath the New Britain region the initial polarization directions of the nulls generally align with fast directions.

Beneath the Philippines, we obtained 20 results, of which 14 are nulls and 6 splits. Of the 14 nulls, 5 are rated "good," 6 "fair," and 3 "poor." We obtained 2 "good," 2 "fair," and 2 "poor" splits. The deepest event that yielded a split arrival originated at 627 km with 1.3 s delay time. Measured delay times ranged from 0.9 s to 1.6 s. Fast directions generally appear to trend perpendicular to the

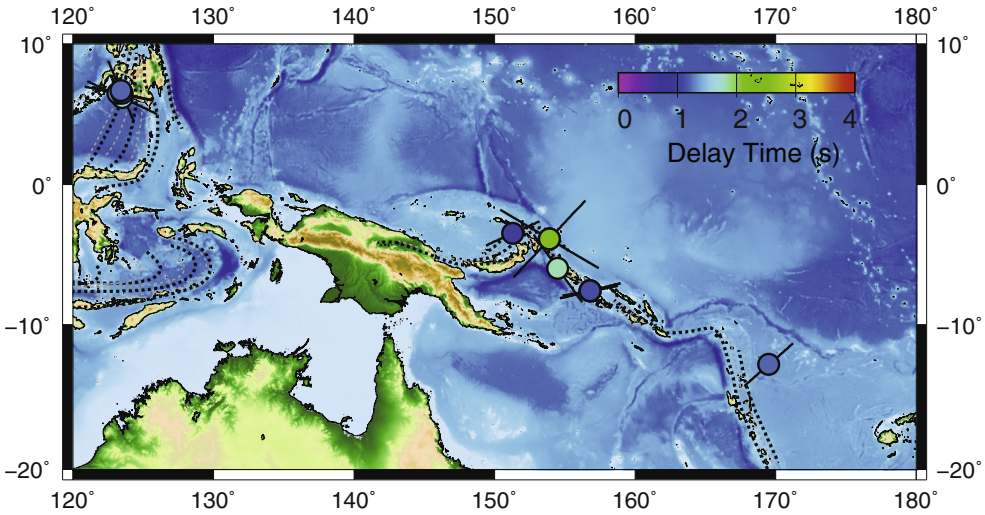

Fig. 9. Splitting results from the New Hebrides, New Britain and Philippines regions. Plotting conventions are as in Fig. 6. For New Hebrides, the deepest slab contour is 400 km; for New Britain, 600 km; for Molucca, 650 km.

Moluccan slab (Fig. 9). As in the case of other areas, measured fast directions and the polarizations of null arrivals are generally consistent with the null polarizations but exhibit more scatter.

5. Discussion

5.1. Comparisons with previous work and global patterns of mid-mantle splitting

Here we discuss the general patterns of mid-mantle shear wave splitting documented in this study and in subduction zones worldwide. For the purpose of this discussion, we combine our results with previously published measurements obtained using identical station selection, receiver side correction techniques, and data processing procedures. These measurements come from the work of Foley and Long (2011) for Tonga, Lynner and Long (2014) for Sumatra and Japan, and Lynner and Long (2015) for Izu-Bonin, Japan-Kuriles, and South America. A schematic diagram summarizing first-order observations from different subduction zones is shown in Fig. 10. Following our own previous work and that of others (e.g., Russo and Silver, 1994; Di Leo et al., 2012; Nowacki et al., 2015), we interpret our measurements as mainly reflecting anisotropy in the mid-mantle near the earthquake

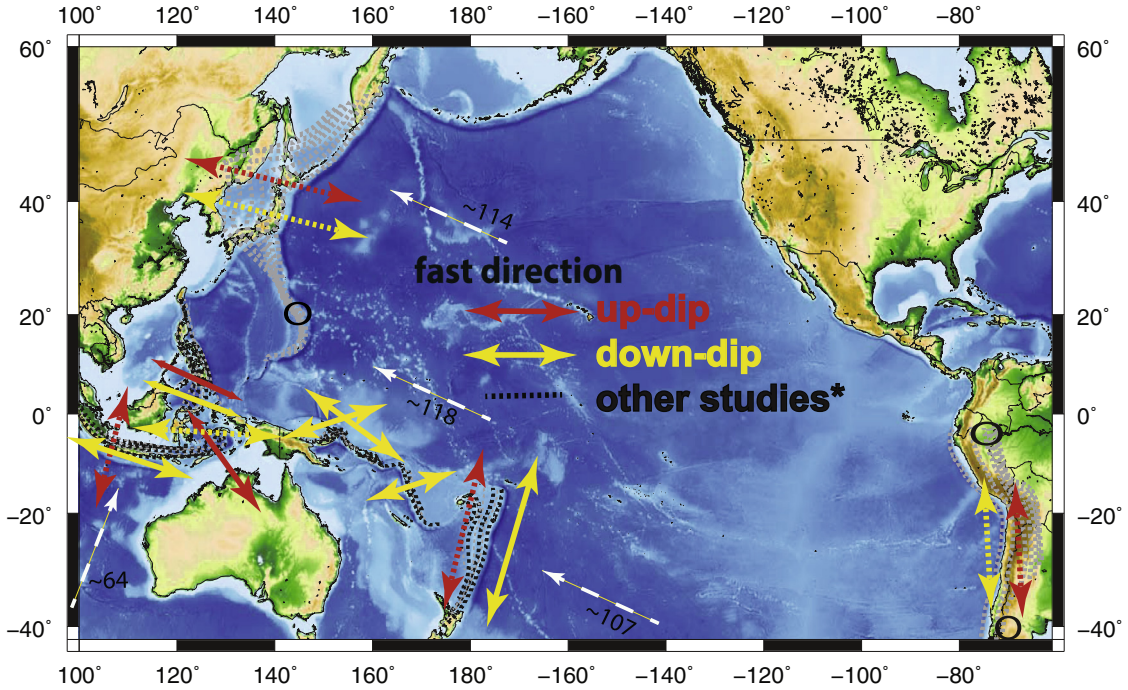

Fig. 10. Schematic diagram of general patterns of fast directions obtained in this study, along with previous measurements documented by Foley and Long (2011) and Lynner and Long (2015). Beneath Tonga, the dominant observed fast directions are mainly trench-parallel for both up-dip and down-dip ray paths. Beneath western Sumatra, dominant fast directions are trench parallel for down-dip ray paths but are trench perpendicular for up-dip ray paths. Eastern Sumatra shows an opposite pattern, with rays traveling in an up-dip direction resulting in trench oblique splitting while those headed down-dip show trench parallel fast directions. Beneath the Philippines, New Hebrides and New Britain, we have only down-dip raypaths, as shown. For central Japan, dominant fast directions are trench perpendicular for both up-dip and down-dip paths. For central South America, that fast direction is trench parallel for both up-dip and down-dip raypaths. 'O' denotes a complex pattern of fast direction (see Lynner and Long, 2015). White dashed arrows show the plate motion direction; rate of movement with respect to Pacific hotspot reference frame is noted in mm/yr.

source, although we cannot completely constrain the lateral extent of the anisotropic loci. We thus assume that (1) our receiver-side correction procedure has accounted for anisotropy in the upper mantle near the station, and (2) the bulk of the lower mantle is isotropic and does not contribute to our measurements. The latter assumption is generally justified based on previous seismological and mineral physics studies (e.g. Meade et al., 1995; Panning and Romanowicz, 2006; Moulik and Ekström, 2014), but we acknowledge that it is difficult to completely rule out a contribution from lower mantle anisotropy far away from the source to our measurements. However, the heterogeneity in the measurements themselves (Figs. 6–9) may argue against a major contribution from the deep lower mantle; if coherent, strong anisotropy in the lower mantle made a significant contribution to our observations, we would expect less heterogeneity.

We observe generally consistent delay times both within individual subduction systems and in the global dataset (Fig. 11), with average delay times for each region ranging from 1.0 to 1.5 s. Notably, we do not observe any striking dependence of measured delay time on event depth, either for the measurements presented in this study (Fig. 11a) or for our quasi-global dataset (Fig. 11b). There is perhaps some hint of a bimodal distribution of delay times for our measurements (Fig. 11), as a few results originating from the top of the transition zone (near ~410 km) and near the bottom of the transition zone (near ~660 km) exhibit particularly large delay times. In contrast, measurements from events originating in the middle portion of the transition zones tend to exhibit uniformly smaller delay times. However, this pattern is dominated by a few measurements with particularly large delay times, and is not statistically significant. Notably, we do not observe any systematic variability in delay times with ray path; we document similar delay times for up-dip vs. down-dip raypaths for systems with good raypath coverage such as Sumatra and Tonga (Fig. 12).

In contrast to the relatively uniform delay times, we document a great deal of variability in fast splitting direction, both within and among subduction systems. Interestingly, however, in most systems the fast directions do not tend to change systematically with depth; rather, they vary spatially. For Tonga, our fast directions are mostly roughly parallel to the trench (Figs. 6 and 13), but there are

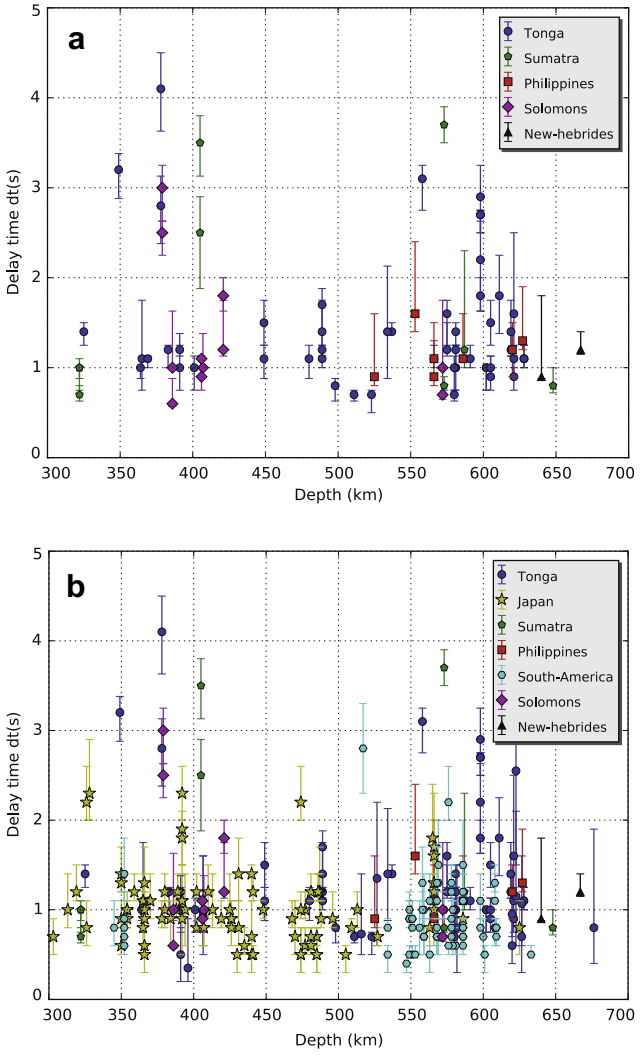

Fig. 11. (a) Plot of delay time vs. depth for measurements presented in this study. Error bars represent the 95% confidence region on each delay time measurement. (b) Same as (a), but data from this study, Lynner and Long (2014, 2015) and Foley and Long (2011) are shown.

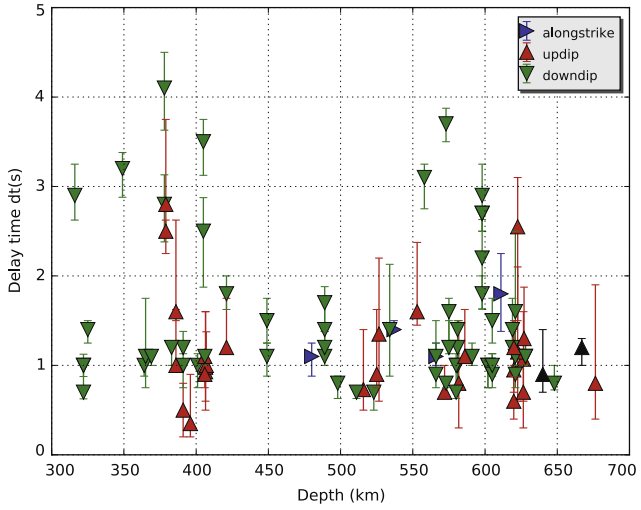

Fig. 12. Delay time vs. depth plot for individual results from this study, sorted by takeoff direction relative to the slab geometry. Inverted green solid triangles represent down-dip raypaths, solid red triangles represent up-dip raypaths and blue triangles represent along-strike raypaths. The black triangles are the measurements for which we cannot classify raypaths clearly as up-dip, down-dip or along strike. The error bars represent the 95% confidence region on the delay time estimates. (For interpretation of the references to color in this figure legend, the reader is referred to the web version of this article.)

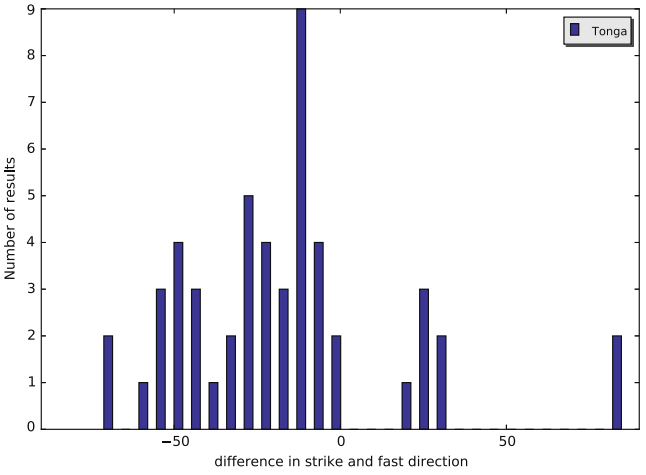

Fig. 13. Histogram of the difference between observed fast directions and local trench strike beneath Tonga from this study and from Foley and Long (2011).

significant departures from this pattern. In particular, our fast directions deviate from trench-parallel where the slab contours bend in the middle portion of the slab (Fig. 6), suggesting that the slab morphology may affect the anisotropy geometry. This pattern is observed for raypaths with a variety of propagation directions, measured at stations in both Japan and Antarctica. We compare these results to previously published measurements for Tonga: Foley and Long (2011) documented mainly trench-parallel to trench-oblique fast directions for a set of raypaths measured in western North America, but their study did not have coverage for the central portion of the Tonga-Kermadec subduction zone. In contrast, Nowacki et al. (2015) reported convergence-parallel fast directions from northern Tonga for a set of raypaths measured in western North America. It is not clear why these measurements disagree with those of Foley and Long (2011), but the discrepancies may reflect complex anisotropy beneath western North America, which would make accurate receiver-side corrections difficult. We further note that Kaneshima (2014) documented small delay times (less than 0.5 s) and mainly null measurements for a set of raypaths measured in Japan for deep events originating in the northernmost portion of the Tonga slab. This is consistent with our documentation of a large number of highly scattered null observations for this region (Fig. 7). This may suggest that rays that mainly sample the mantle to the north of the northern edge of the Tonga slab are primarily sampling isotropic mid-mantle structure; the anisotropy may be confined to the mantle directly surrounding the slab and not extend past the slab edge.

For Sumatra and the Philippines, our results are also generally consistent with previous work by Di Leo et al. (2012) and Nowacki et al. (2015). We document very similar delay times in these systems; furthermore, we observe similar trench oblique and trench-perpendicular fast directions in the Philippines and western Sumatra respectively as documented by Di Leo et al. (2012) and Nowacki et al. (2015). In addition, the polarizations of the "good" quality null measurements are sub-parallel to direct S fast splitting directions in both subduction zones (Fig. S3). We compare our results for Sumatra (Fig. 8) with the previous results of Lynner and Long (2014), which focused exclusively on up-dip raypaths. In contrast, the results presented here focus on down-dip raypaths. Lynner and Long (2014) documented trench-perpendicular fast directions in eastern Sumatra and trench-parallel fast directions beneath western Sumatra for up-dip raypaths. In contrast, down-dip rays experience the opposite splitting pattern, with trench-parallel φ to the east and trench-perpendicular φ to the west (Fig. 10). Rays taking off in a down-dip direction, in addition to sampling mantle around the Sumatra slab, may also encounter other subducting slabs such as the Moluccan slab to the north, potentially complicating the splitting pattern. However, the observed delay times are similar for both up-dip and down-dip raypaths.

We note that in many of the subduction zones we examined, we found a laterally varying pattern in fast direction. In some cases, the pattern of lateral variability appears to follow the contours of the slab in the mid-mantle, as in case of Tonga (Fig. 6) and some parts of New Britain (Fig. 9). For these regions, this may suggest that the morphology of the slab in the mid-mantle plays a role in the development of anisotropy, either by controlling the geometry of mid-mantle flow or by controlling the orientation of anisotropy within the slab itself. For other regions, however, particularly Sumatra, the lateral variability in fast directions does not appear to correlate with variations in slab morphology. We note, as well, that for regions such as the Philippines and New Hebrides, we do not have sufficient along-strike sampling to constrain lateral variability. Finally, we emphasize that while many of the subduction systems examined exhibit along-strike variability in φ, we do not observe any systematic variability in φ with depth.

5.2. Possible sources of anisotropy

There are three potential contributions to shear wave splitting measured at the station: anisotropy in the upper mantle beneath the station on the receiver side, anisotropy within the slab itself close to the source, and anisotropy in the mantle surrounding the slab due to mantle deformation (e.g., Long and Becker, 2010). Since our analysis procedure accounts for any receiver side anisotropy, our measurements therefore likely reflect anisotropy on the source side, but both the slab and the surrounding mantle may potentially contribute. Anisotropy within subducting slabs may be due to frozen-in anisotropy in the lithospheric mantle, CPO and/or SPO of serpentinite minerals, and/or CPO of dense super-hydrous phases (e.g., Long, 2013; Nowacki et al., 2015). Because our data are sensitive to anisotropy at depths below 300 km, we can rule out a contribution from serpentinized mantle, as serpentine minerals are not stable beyond depths of ~100 km (Ulmer and Trommsdorff, 1995).

The "frozen in anisotropy" model suggests that anisotropic structure is created in the asthenosphere due to olivine CPO induced by shearing with the overriding lithosphere during seafloor spreading; this structure is then frozen in as the lithosphere cools. If our splitting measurements mainly reflected frozen anisotropy due to metastable olivine CPO in the lithospheric mantle of the slab, then we would expect to observe fast directions that are controlled by the fossil spreading direction of the oceanic lithosphere, and the observations should be consistent among different subduction zones with similar fossil spreading directions. This prediction is not borne out by our observations, however. This model would suggest similar fast directions for Tonga and Japan, for example, which is not observed (Fig. 10). In addition, in New Britain, we observe a variable pattern of φ even though the fossil spreading direction likely does not vary much. Therefore, we rule out this mechanism as the primary contribution to our observations.

Super-hydrous phases such as phase B or phase D can potentially contribute to the anisotropic structure within the slab (e.g., Rosa et al., 2013; Nowacki et al., 2015). Super-hydrous phase B, with a shear wave anisotropy of 11.6%, is stable only at transition zone conditions and has an intrinsic anisotropy less than that of wadsleyite but higher than that of ringwoodite (Mainprice and Ildefonse, 2009). Phase D is stable beyond transition zone depths, has intrinsic Vs anisotropy of ~18% (Mainprice and Ildefonse, 2009), and may form texture when deformed (Rosa et al., 2013). In order for these phases to make a primary contribution to our splitting measurements (with average delay times up to ~1.5 s), however, they must be volumetrically important. Simple one-dimensional ray tracing using TauP shows that many of our direct S rays do not have long path lengths through the slab (generally ~30–40 km, although in places where the slab dip and ray take off angle are similar, the ray travels along the length of the slab, ~100 km), in contrast to the surrounding mantle (several 100's of km). A simple calculation assuming single-crystal anisotropy of phase B (phase D) and a ~50 km ray path through the slab would suggest that a volume percentage of phase B of 80% (55% for phase D) would be required to explain our observed delay times. Such high volumetric percentage of these phases is unlikely even under a water-saturated slab environment (Ohtani et al., 2004); furthermore, the anisotropy of a phase B or phase D aggregate would likely be weaker than the single-crystal case. Another argument against a primary contribution from anisotropy within the slab itself comes from the observations: our dataset contains a few raypaths with long slab path lengths (~100 km, as mentioned above), and these do not exhibit consistently larger delay times than down-dip raypaths with much shorter slab paths (Fig. 12). As these combined lines of evidence suggest that a primary

contribution from slab anisotropy is unlikely, and since the bulk of the lower mantle is thought to be isotropic (Meade et al., 1995), the most likely source for the anisotropy is in the mantle surrounding the subducting slabs near the earthquake sources (Fig. 2).

An important question is whether our measurements mainly reflect anisotropy from the upper transition zone, lower transition zone, the uppermost lower mantle, or a combination. Recent work on the depth dependence of transition zone anisotropy by Yuan and Beghein (2013) has produced evidence for changes in anisotropic geometry and strength across the transition zone phase changes, suggesting potential contributions from several different phases and depth ranges. Because we observe significant splitting (delay times >1 s) for S phases originating from earthquakes at the base of the transition zone in several subduction systems, our observations seem to require a significant contribution from the uppermost lower mantle. Furthermore, the fact that we do not observe a marked decrease in delay time with depth (Fig. 10) suggests that anisotropy in the upper part of the lower mantle likely makes the primary contribution to our observations, although there may be a contribution from transition zone anisotropy as well. As a simple exercise, we calculated the length of typical raypaths traveling through the transition zone and the lower mantle and estimated the strength of anisotropy needed to explain our delay times. For a typical delay time of 1 s, assuming the region of deformation of mantle around the slab to be ~200 km thick, we need about 5% anisotropy for rays traveling through the uppermost lower mantle. The strength of anisotropy and the thickness of the layer trade off directly, so a thicker layer would allow for weaker anisotropy, and vice versa. The likely strength of CPO in bridgmanite deformed via dislocation creep is poorly known, but future experiments may shed light on whether an anisotropic strength of ~5% in the uppermost lower mantle is plausible.

5.3. Implications for mid-mantle deformation

Previous studies have cited a dearth of observations of seismic anisotropy at depths below 300 km as evidence for deformation accommodated in the diffusion creep regime (e.g., Karato and Wu, 1993). Recently, however, there have been convincing observations of anisotropy at transition zone and uppermost lower mantle depths, using both surface wave (Trampert and van Heijst, 2002; Yuan and Beghein, 2013) and body wave (Wookey et al., 2002; Foley and Long, 2011; Di Leo et al., 2012; Lynner and Long, 2014, 2015; Nowacki et al., 2015) observations. The robust anisotropy signal documented in these previous papers, as well as in the present study, indicates the presence of either CPO or SPO in the mid-mantle. Studies of the relationships between strain and the resulting CPO are in their infancy for transition zone minerals and these relationships remain almost completely unknown for uppermost lower mantle minerals, owing to experimental difficulties to reach the deformation conditions of the lower mantle. Preliminary experiments by Kawazoe et al. (2013) show that at 1800 K, wadsleyite deforms via dislocation creep dominated by the [001](010) slip system. Other slip systems, however, have also been proposed based on stress relaxation tests (Thurel et al., 2003). More recently, Ohuchi et al. (2014) showed that the CPO in wadsleyite changes with water content, and that CPO strength in wadsleyite may be modest. Cordier et al. (2004) experimentally demonstrated that when bridgmanite deforms in dislocation creep regime CPO develops, but since uppermost lower mantle has ~20% ferropericlase, strain partitioning between these two phases needs to be determined before we attribute anisotropy to a particular phase.

Only a few geodynamical modeling studies have directly addressed the question of deformation and anisotropy in the mid-mantle. Based on a series of fully dynamic models of subducting slabs and flow in the surrounding mantle, Faccenda (2014) suggested that considerable anisotropy may develop in the mid-mantle if the transition stress for a change in deformation mechanism from diffusion creep to dislocation creep is approximately 10 MPa. His models suggest that a slab impinging on a high-viscosity lower mantle may induce stresses above this threshold, causing materials to deform in the dislocation creep regime and producing anisotropy. His study considered various models based on a variety of subduction rates and behavior of slabs stagnating in the transition zone, and found that the predicted anisotropy pattern should be similar across all parameters considered. Based on these results, Faccenda (2014) proposed that the upper transition zone would have weaker anisotropy because of low strain and the presence of phase transformations that reset the CPO. In contrast, the uppermost lower mantle would exhibit strong deformation and large strains; in combination with a larger modal abundance of a strongly anisotropic phase (bridgmanite), this would result in stronger anisotropy.

Our inference of significant mid-mantle anisotropy in most subduction systems, with a significant contribution from the uppermost lower mantle, is consistent with this suggestion. However, we observe a wider diversity of measured fast splitting directions than suggested by Faccenda (2014) models. For example, Faccenda (2014) explains the deep trench parallel anisotropy fast directions beneath Tonga documented by Foley and Long (2011) based on the deformation of bridgmanite via the [010](100) slip system. The models of Faccenda (2014) might predict similar deformation geometry and dominant slip systems for other similar Subduction systems, such as Japan, which also exhibits slab stagnation in the mid-mantle (Fukao and Obayashi, 2013). Our global compilation, however, suggests greater diversity in observed fast directions than predicted by simple models; in particular, beneath Japan Lynner and Long (2015) documented mostly trench-perpendicular fast directions. We speculate that this may be consistent with a fabric transition due to different deformation conditions, or due to a difference in deformation style or geometry, perhaps due to different interactions with the lower mantle. However, a dearth of experimental data on the deformation mechanisms of transition zone and lower mantle minerals hampers our ability to interpret our measurements in terms of flow patterns. Another factor to consider is that deformation history may introduce lag between the fabric development and deformation kinematics, at least in upper mantle minerals (e.g., Skemer et al., 2012); this is likely true for the mid-mantle as well.

5.4. Splitting patterns, trench migration rates, and slab morphology in the mid-mantle

An important kinematic factor that may affect the deformation of slabs in the mid-mantle is the migration of the trench (advance or retreat) in a mantle reference frame. Trench migration has been shown to be important for the development of upper mantle anisotropy in subduction systems, both in the mantle wedge above the slab and in the sub-slab mantle (e.g., Long and Becker, 2010; Long, 2013). Migrating trenches create a three-dimensional flow field that is more complex than a simple two-dimensional model of entrained flow would predict; the resulting flow fields have a significant toroidal component and create complicated finite strain and anisotropy patterns (e.g., Druken et al., 2011; Faccenda, 2014; Leo et al., 2014; Paczkowski et al., 2014). Another reason trench migration is important is that it is likely connected to the geometry of slabs in the transition zone; one model for stagnant slabs in the mid-mantle is that slabs become anchored in the high-viscosity lower mantle and the slower sinking forces the trench to roll back (e.g., Billen, 2010).

Table 1
Table summarizing mid-mantle splitting patterns from this study and from previous works, along with relevant subduction parameters. Shown are the age of the downgoing plate at the trench (Heuret and Lallemand, 2005), trench migration rate (Heuret and Lallemand, 2005; Schellart et al., 2008), and the geometry of the slab in mid-mantle as inferred from tomography (Fukao and Obayashi, 2013).

Subduction zone	Age	Trench advance or retreat	Stagnant or non stagnant	Fast direction (trench parallel or perpendicular)
Northern Tonga	110 Myr	Retreat (>100 mm/yr)	Stagnant	Parallel
Southern Tonga	100 Myr	Advance (>40 mm/yr)	Non-stagnant	Parallel
New Hebrides	45 Myr	Retreat (~60 mm/yr)		Perpendicular
New Britain	31 Myr	Advance (10 mm/yr)		Parallel
Western Sumatra	60 Myr	Retreat (15 mm/yr)	Non-stagnant	Down-dip parallel, up-dip perpendicular
Eastern Sumatra	80 Myr	Retreat (15 mm/yr)	Non-stagnant	Up-dip parallel, down-dip perpendicular
Philippines	20 Myr	Advance (25 mm/yr)	Non-stagnant	Perpendicular
South America	48 Myr	Advance (30 mm/yr)	Non-stagnant	Parallel
Japan	135 Myr	Advance (40–50 mm/yr)	Stagnant	Perpendicular

We compiled rates of trench migration for each of the subduction systems in our dataset from Heuret and Lallemand (2005) and Schellart et al. (2008) for a Pacific hotspot reference frame (Table 1) and considered whether there is any correlation between trench migration behavior (advance or retreat) and/or migration rates and the measured splitting patterns. We also considered potential correlations with parameters such as the age of the subducting plate and the geometry and behavior of the slab in the mid-mantle (i.e. stagnant vs. non-stagnant slabs; see Fukao and Obayashi, 2013). As shown in Table 1, there are no obvious, simple relationships between the dominant fast direction observations and the subduction-related parameters that we considered. In particular, the behavior of the slab in the mid-mantle (stagnant in the transition zone, stagnant in the mid-mantle, or easily penetrating into the lower mantle) does not seem to correlate simply with the geometry of anisotropy. This suggests that either there is some complexity in the deformation mechanisms and/or CPO geometry of mid-mantle minerals, or that mid-mantle deformation in subduction systems is highly heterogeneous and the resulting anisotropy patterns are complex, or both.

6. Summary

We analyzed direct S arrivals from deep earthquakes in subducting slabs to characterize the pattern of source-side anisotropy in the mid-mantle in Subduction systems in the southwestern Pacific. We documented evidence for anisotropy at mid-mantle depths (transition zone and uppermost lower mantle) near each of the regions examined in this study. The geometry of anisotropy varies among different subduction systems as well as within individual regions, although the measured delay times are generally uniform. We do not observe a convincing relationship between event depth and delay time, which suggests that the primary source of the anisotropy may be in the uppermost lower mantle. A simple calculation suggests that our delay time observations can generally be explained with a layer of ~5% anisotropy with thickness ~200 km in the mid-mantle. We interpret our measurements as mainly reflecting the deformation of the ambient mantle surrounding the subducting slab, with a primary contribution from the CPO of bridgmanite. Our preferred interpretation contrasts with that of Nowacki et al. (2015), who suggested that mid-mantle anisotropy in subduction systems is mainly due to hydrous phases stable at high pressure within the slab itself. Our interpretation is generally consistent, however, with recent numerical experiments on mid-mantle deformation in subduction systems (Faccenda, 2014). We combined our measurements with previously published results obtained using identical measurement procedures to produce a quasi-global dataset of source-side splitting measurement from deep earthquakes. Using this combined dataset, we evaluated possible correlations between the geometry of splitting and a variety of parameters that describe subduction, such as trench migration and plate age. We identified no systematic correlations with subduction parameters, however. We suggest that our measurements reflect generally heterogeneous deformation associated with the impingement of subducting slabs onto a higher viscosity layer in the mid-mantle. Future work on deformation mechanisms and fabric development in mid-mantle materials will allow for the interpretation of our measurements in terms of flow patterns.

Acknowledgments

This work was supported via NSF grant EAR-1150722. We used seismic data from the following networks: Global Seismograph Network (II, IU), F-net, Japan Meteorological Agency Seismic Network (JP), China Digital Seismograph Network (CD), New China Digital Seismograph Network (IC), Geoscience Australia (AU), GEOSCOPE (G), Pacific21 (PS), Kazakhstan Network (KZ). Data were accessed via the Data Management System (DMS) of the Incorporated Research Institutions for Seismology (IRIS) or via the Japanese National Research Institute for Earth Science and Disaster Prevention data center. Figures were prepared with GMT (Wessel and Smith, 1991). We are grateful to Shun Karato for helpful discussions on the anisotropy of mid-mantle minerals, and to Manuele Faccenda and an anonymous reviewer for constructive comments that improved the paper.

Appendix A. Supplementary data

Supplementary data associated with this article can be found, in the online version, at http://dx.doi.org/10.1016/j.pepi.2015.05.003.

References

Anderson, D.L., 1967. Phase changes in upper mantle. Science 157, 1165–1173.
Bass, J.D., Parise, J.B., 2008. Deep earth and recent developments in mineral physics. Elements 4, 157–163.
Billen, M.I., 2010. Slab dynamics in the transition zone. Phys. Earth Planet. Inter. 183, 296–308. http://dx.doi.org/10.1016/j.pepi.2010.05.005.
Bird, P., 2003. An updated digital model of plate boundaries. Geochem. Geophys. Geosyst. 4, 1027. http://dx.doi.org/10.1029/2001GC000252.
Chen, W.-P., Brudzinski, M.R., 2003. Seismic anisotropy in the mantle transition zone beneath Fiji-Tonga. Geophys. Res. Lett. 30 (1682), 2002G. http://dx.doi.org/10.1029/L016330.
Cordier, P., Ungar, T., Zsoldos, L., Tichy, G., 2004. Dislocation creep in $MgSiO_3$ perovskite at conditions of the Earth's uppermost lower mantle. Nature 428, 837–840.
Demouchy, S., Mainprice, D., Tommasi, A., Couvy, H., Barou, F., Frost, D.J., Cordier, P., 2011. Forsterite to wadsleyite phase transformation under shear stress and consequences for the Earth's mantle transition zone. Phys. Earth Planet. Inter. 184, 91–104. http://dx.doi.org/10.1016/j.pepi.2010.11.001.
Di Leo, J.F., Wookey, J., Hammond, J.O.S., Kendall, J.M., Kaneshima, S., Inoue, H., Yamashina, T., Harjadi, P., 2012. Mantle flow in regions of complex tectonics: insights from Indonesia. Geochem. Geophys. Geosyst. 13, Q12008. http://dx.doi.org/10.1029/2012GC004417.
Druken, K.A., Long, M.D., Kincaid, C., 2011. Patterns in seismic anisotropy driven by rollback subduction beneath the High Lava Plains. Geophys. Res. Lett. 38, L13310. http://dx.doi.org/10.1029/2011GL047541.

Faccenda, M., 2014. Mid mantle seismic anisotropy around subduction zones. Phys. Earth Planet. Inter. 227, 1–19. http://dx.doi.org/10.1016/j.pepi.2013.11.015.

Foley, B.J., Long, M.D., 2011. Upper and mid-mantle anisotropy beneath the Tonga slab. Geophys. Res. Lett. 38, L02303. http://dx.doi.org/10.1029/2010GL046021.

Fukao, Y., Obayashi, M., 2013. Subducted slabs stagnant above, penetrating through, and trapped below the 660 km discontinuity. J. Geophys. Res. Solid Earth 118, 5920–5938. http://dx.doi.org/10.1002/2013JB010466.

Fukao, Y., Obayashi, M., Inoue, H., Nenbai, M., 1992. Subducting slabs stagnant in the mantle transition zone. J. Geophys. Res. Solid Earth 97, 4809–4822. http://dx.doi.org/10.1029/91JB02749.

Gripp, A.E., Gordon, R.G., 2002. Young tracks of hot spots and current plate velocities. Geophys. J. Int. 150, 321–361. http://dx.doi.org/10.1046/j.1365-246X.2002.01627.x.

Gudmundsson, O., Sambridge, M., 1998. A regionalized upper mantle (RUM) seismic model. J. Geophys. Res. Solid Earth 103, 7121–7136. http://dx.doi.org/10.1029/97JB02488.

Hall, R., Spakman, W., 2003. Mantle structure and tectonic evolution of the region north and east of Australia. Special Papers of the Geological Society of America, pp. 361–382, <http://dx.doi.org/10.1130/0-8137-2372-8.361>.

He, X., Long, M.D., 2011. Lowermost mantle anisotropy beneath the northwestern Pacific: evidence from PcS, ScS, SKS, and SKKS phases. Geochem. Geophys. Geosyst. 12, Q12012. http://dx.doi.org/10.1029/2011GC003779.

Heuret, A., Lallemand, S., 2005. Plate motions, slab dynamics and back-arc deformation. Phys. Earth Planet. Inter. 149, 31–51. http://dx.doi.org/10.1016/j.pepi.2004.08.022.

Kaneshima, S., 2014. Upper bounds of seismic anisotropy in the Tonga slab near deep earthquake foci and in the lower mantle. Geophys. J. Int. 197, 351–368. http://dx.doi.org/10.1093/gji/ggt494.

Karason, H., van der Hilst, R.D., 2000. Constraints on mantle convection from seismic tomography. Geophys. Monogr. Ser. 121, 277–288. http://dx.doi.org/10.1029/ GM121p0277.

Karato, S., Wu, P., 1993. Rheology of the upper mantle – a synthesis. Science 260, 771–778.

Karato, S., Jung, H., Katayama, I., Skemer, P., 2008. Geodynamic significance of seismic anisotropy of the upper mantle: new insights from laboratory studies. Annu. Rev. Earth Planet. Sci. 36, 59–95. http://dx.doi.org/10.1146/annurev.earth.36.031207.124120.

Karki, B.B., Stixrude, L., Clark, S.J., Warren, M.C., Ackland, G.J., Crain, J., 1997. Elastic properties of orthorhombic $MgSiO_3$ perovskite at lower mantle pressures. Am. Mineral. 82, 635–638.

Karki, B.B., Stixrude, L., Wentzcovitch, R.M., 2001. High-pressure elastic properties of major materials of Earth's mantle from first principles. Rev. Geophys. 39, 507–534. http://dx.doi.org/10.1029/2000RG000088.

Kawazoe, T., Ohuchi, T., Nishihara, Y., Nishiyama, N., Fujino, K., Irifune, T., 2013. Seismic anisotropy in the mantle transition zone induced by shear deformation of wadsleyite. Phys. Earth Planet. Inter. 216, 91–98. http://dx.doi.org/10.1016/j.pepi.2012.12.005.

Leo, J., Walker, A., Li, Z.H., Wookey, J., Ribe, N., Kendall, J.M., Tommasi, A., 2014. Development of texture and seismic anisotropy during the onset of subduction. Geochem. Geophys. Geosyst. 15, 192–212. http://dx.doi.org/10.1002/2013GC005032.

Li, L., Weidner, D.J., Brodholt, J., Alfè, D., Price, G.D., 2006. Elasticity of Mg_2SiO_4 ringwoodite at mantle conditions. Phys. Earth Planet. Inter. 147, 181–187. http://dx.doi.org/10.1016/j.pepi.2006.04.002.

Long, M.D., 2013. Constraints on subduction geodynamics from seismic anisotropy. Rev. Geophys. 51, 76–112. http://dx.doi.org/10.1002/rog.20008.

Long, M.D., Becker, T.W., 2010. Mantle dynamics and seismic anisotropy. Earth Planet. Sci. Lett. 297, 341–354. http://dx.doi.org/10.1016/j.epsl.2010.06.036.

Long, M.D., van der Hilst, R.D., 2005. Upper mantle anisotropy beneath Japan from shear wave splitting. Phys. Earth Planet. Inter. 151, 206–222. http://dx.doi.org/10.1016/j.pepi.2005.03.003.

Lynner, C., Long, M.D., 2013. Sub-slab seismic anisotropy and mantle flow beneath the Caribbean and Scotia subduction zones: effects of slab morphology and kinematics. Earth Planet. Sci. Lett. 361, 367–378. http://dx.doi.org/10.1016/j.epsl.2012.11.007.

Lynner, C., Long, M.D., 2014. Sub-slab anisotropy beneath the Sumatra and circum-Pacific subduction zones from source-side shear wave splitting observations. Geochem. Geophys. Geosyst. 15, 2262–2281. http://dx.doi.org/10.1002/2014GC005239.

Lynner, C., Long, M.D., 2015. Heterogeneous seismic anisotropy in the transition zone and uppermost lower mantle: evidence from South America, Izu-Bonin, and Japan. Geophys. J. Int. 201, 1522–1545. http://dx.doi.org/10.1093/gji/ggv099.

Mainprice, D., 2007. Seismic anisotropy of the deep Earth from a mineral and rock physics perspective. Treatise of Geophysics, 2. Elsevier. http://dx.doi.org/10.1016/B978-044452748-6.00045-6, 437-491.

Mainprice, D., Ildefonse, B., 2009. Seismic Anisotropy of Subduction Zone Minerals–contribution of Hydrous Phases, Subduction Zone Geodynamics. Springer, USA, pp. 63–84.

Mainprice, D., Barruol, G., Ismail, W.B., 2000. The seismic anisotropy of the Earth's mantle: from single crystal to polycrystal. In: Earth's Deep Interior: Mineral Physics and Tomography from the Atomic to the Global Scale, pp. 237–264, <http://dx.doi.org/10.1029/GM117p0237>.

Mao, Z., Jacobsen, S.D., Jiang, F., Smyth, J.R., Holl, C.M., Frost, D.J., Duffy, T.S., 2008. Single crystal elasticity of wadselyites, b-Mg_2SiO_4 containing 0.37–1.66 wt% H_2O. Earth Planet. Sci. Lett. 266, 78–79. http://dx.doi.org/10.1016/j.epsl.2007.10.045.

Marquardt, H., Speziale, S., Reichmann, H.J., Frost, D.J., Schilling, F.R., Garnero, E.J., 2009. Elastic shear anisotropy of ferropericlase in Earth's lower mantle. Science 324, 224–226.

McNamara, A.K., van Keken, P.E., Karato, S.-I., 2003. Development of finite strain in the convecting lower mantle and its implications for seismic anisotropy. J. Geophys. Res. Solid Earth 108, 2230. http://dx.doi.org/10.1029/2002JB001970.

Meade, C., Silver, P.G., Kaneshima, S., 1995. Laboratory and seismological observations of lower mantle isotropy. Geophys. Res. Lett. 22, 1293–1296. http://dx.doi.org/10.1029/95GL01091.

Moulik, P., Ekström, G., 2014. An anisotropic shear velocity model of the Earth's mantle using normal modes, body waves, surface waves, and long-period waveforms. Geophys. J. Int. 199, 1713–1738. http://dx.doi.org/10.1093/gji/ggu356.

Müller, R.D., Sdrolias, M., Gaina, C., Roest, W.R., 2008. Age, spreading rates, and spreading asymmetry of the world's ocean crust. Geochem. Geophys. Geosyst. 9, Q04006. http://dx.doi.org/10.1029/2007GC001743.

Nowacki, A., Kendall, J.-M., Wookey, J., Pemberton, A., 2015. Mid-mantle anisotropy in subduction zones and deep water transport. Geochem. Geophys. Geosyst. 16, 764–784. http://dx.doi.org/10.1002/2014GC005667.

Ohtani, E., Litasov, K., Hosoya, T., Kubo, T., Kondo, T., 2004. Water transport into the deep mantle and formation of a hydrous transition zone. Phys. Earth Planet. Inter. 143, 255–269. http://dx.doi.org/10.1016/j.pepi.2003.09.015.

Ohuchi, T., Fujino, K., Kawazoe, T., Irifune, T., 2014. Crystallographic preferred orientation of wadsleyite and ringwoodite: effects of phase transformation and water on seismic anisotropy in the mantle transition zone. Earth Planet. Sci. Lett. 397, 133–144. http://dx.doi.org/10.1016/j.epsl.2014.03.066.

Paczkowski, K., Thissen, C.J., Long, M.D., Montési, L.G., 2014. Deflection of mantle flow beneath subducting slabs and the origin of subslab anisotropy. Geophys. Res. Lett. 41, 6734–6742. http://dx.doi.org/10.1002/2014GL060914.

Panning, M., Romanowicz, B., 2006. A three-dimensional radially anisotropic model of shear velocity in the whole mantle. Geophys. J. Int. 167, 361–379. http://dx.doi.org/10.1111/j.1365-246X.2006.03100.x.

Rosa, A.D., Sanchez-Valle, C., Nisr, C., Evans, S.R., Debord, R., Merkel, S., 2013. Shear wave anisotropy in textured phase D and constraints on deep water recycling in subduction zones. Earth Planet. Sci. Lett. 377, 13–22. http://dx.doi.org/10.1016/j.epsl.2013.06.036.

Russo, R.M., Silver, P.G., 1994. Trench-parallel flow beneath the Nazca Plate from seismic anisotropy. Science 263, 1105–1111.

Russo, R.M., Gallego, A., Comte, D., Moncau, V.I., Murdie, R.E., VanDecar, J.C., 2010. Source-side shear wave splitting and upper mantle flow in the Chile Ridge subduction zone. Geology 38, 707–710.

Savage, M.K., 1999. Seismic anisotropy and mantle deformation: what have we learned from shear wave splitting? Rev. Geophys. 37, 65–106. http://dx.doi.org/10.1029/98RG02075.

Schellart, W.P., Stegman, D.R., Freeman, J., 2008. Global trench migration velocities and slab migration induced upper mantle volume fluxes: constraints to find an Earth reference frame based on minimizing viscous dissipation. Earth Sci. Rev. 88, 118–144. http://dx.doi.org/10.1016/j.earscirev.2008.01.005.

Silver, E.A., Moore, J.C., 1978. The Molucca Sea collision zone, Indonesia. J. Geophys. Res. 83, 1681–1691. http://dx.doi.org/10.1029/JB083iB04p01681.

Skemer, P., Warren, J.M., Hirth, G., 2012. The influence of deformation history on the interpretation of seismic anisotropy. Geochem. Geophys. Geosyst. 13, Q03006. http://dx.doi.org/10.1029/2011GC003988.

Smyth, J.R., Miyajima, N., Huss, G.R., Hellebrand, E., Rubie, D.C., Frost, D.J., 2012. Olivine–wadsleyite–pyroxene topotaxy: evidence for coherent nucleation and diffusion-controlled growth at the 410-km discontinuity. Phys. Earth Planet. Inter. 200, 85–91. http://dx.doi.org/10.1016/j.pepi.2012.04.003.

Thurel, E., Douin, J., Cordier, P., 2003. Plastic deformation of wadsleyite: III. Interpretation of dislocations and slip systems. Phys. Chem. Miner. 30, 271–279. http://dx.doi.org/10.1007/s00269-003-0314-6.

Trampert, J., van Heijst, H.J., 2002. Global azimuthal anisotropy in the transition zone. Science 296, 1297–1299.

Tschauner, O., Ma, C., Beckett, J.R., Prescher, C., Prakapenka, V.B., Rossman, G.R., 2014. Discovery of bridgmanite, the most abundant mineral in Earth, in a shocked meteorite. Science 346, 1100–1102.

Ulmer, P., Trommsdorff, V., 1995. Serpentine stability to mantle depths and subduction-related magmatism. Science 268, 858–861.

van der Hilst, R., 1995. Complex morphology of subducted lithosphere in the mantle beneath the Tonga trench. Nature 374, 154–157.

van der Hilst, R.D., Engdahl, R., Spakman, W., Nolet, G., 1991. Tomographic imaging of subducted lithosphere below Northwest Pacific island arcs. Nature 353, 37–43.

Vinnik, L.P., Kind, R., 1993. Ellipticity of teleseismic S-particle motion. Geophys. J. Int. 113, 165–174. http://dx.doi.org/10.1111/j.1365-246X.1993.tb02537.x.

Wang, J.S., Sinogeikin, V., Inoue, T., Bass, J.D., 2006. Elastic properties of hydrous ringwoodite at high-pressure conditions. Geophys. Res. Lett. 33, L14308. http://dx.doi.org/10.1029/2006GL026441.

Wenk, H.R., Ischia, G., Nishiyama, N., Wang, Y., Uchida, T., 2005. Texture development and deformation mechanisms in ringwoodite. Phys. Earth Planet. Inter. 152, 191–199. http://dx.doi.org/10.1016/j.pepi.2005.06.008.

Wenk, H.R., Speziale, S., McNamara, A.K., Gamero, E.J., 2006. Modeling lower mantle anisotropy development in a subducting slab. Earth Planet. Sci. Lett. 245, 302–314. http://dx.doi.org/10.1016/j.epsl.2006.02.028.

Wentzcovitch, R.M., Karki, B.B., Cococcioni, M., de Gironcoli, S., 2004. Thermoelastic properties of $MgSiO_3$-perovskite: insights on the nature of the Earth's lower mantle. Phys. Rev. Lett. 92, 018501. http://dx.doi.org/10.1103/PhysRevLett.92.018501.

Wessel, P., Smith, W.H., 1991. Free software helps map and display data. Eos. Trans. Am. Geophys. Union 72, 441–446.

Widiyantoro, S., van der Hilst, R., 1997. Mantle structure beneath Indonesia inferred from high-resolution tomographic imaging. Geophys. J. Int. 130, 167–182. http://dx.doi.org/10.1111/j.1365-246X.1997.tb00996.x.

Wookey, J., Kendall, J.M., 2004. Evidence of midmantle anisotropy from shear wave splitting and the influence of shear-coupled P waves. J. Geophys. Res. Solid Earth 109, B07309. http://dx.doi.org/10.1029/2003JB002871.

Wookey, J., Kendall, J.-M., Barruol, G., 2002. Mid-mantle deformation inferred from seismic anisotropy. Nature 415, 777–780.

Wüstefeld, A., Bokelmann, G., Zaroli, C., Barruol, G., 2008. SplitLab: a shear-wave splitting environment in Matlab. Comput. Geosci. 34, 515–528.

Yuan, K.Q., Beghein, C., 2013. Seismic anisotropy changes across upper mantle phase transitions. Earth Planet. Sci. Lett. 374, 132–144. http://dx.doi.org/10.1016/ j.epsl.2013.05.031.

Zha, C.S., Duffy, T.S., Mao, H.K., Downs, R.T., Hemley, R.J., Weidner, D.J., 1997. Single-crystal elasticity of beta-Mg_2SiO_4 to the pressure of the 410 km seismic discontinuity in the Earth's mantle. Earth Planet. Sci. Lett. 147 (E9–190), E15. http://dx.doi.org/10.1016/S0012-821X(97)00010-1.